

## Transition to turbulence in a five-mode Galerkin truncation of two-dimensional magnetohydrodynamics

Francesco Carbone <sup>\*</sup>

*National Research Council - Institute of Atmospheric Pollution Research, C/o University of Calabria, 87036 Rende, Italy*

Daniele Telloni

*National Institute for Astrophysics - Astrophysical Observatory of Torino, Via Osservatorio 20, 10025 Pino Torinese, Italy*

Gary Zank 

*Center for Space Plasma and Aeronomic Research (CSPAR), University of Alabama in Huntsville, Huntsville, Alabama 35899, USA and Department of Space Science, University of Alabama in Huntsville, Huntsville, Alabama 35899, USA*

Luca Sorriso-Valvo 

*Swedish Institute of Space Physics, Ångström Laboratory, Lägerhyddsvägen 1, SE-751 21 Uppsala, Sweden and CNR, Istituto per la Scienza e Tecnologia dei Plasmi, Via Amendola 122/D, 70126 Bari, Italy*



(Received 19 April 2021; accepted 9 July 2021; published 3 August 2021)

The chaotic dynamics of a low-order Galerkin truncation of the two-dimensional magnetohydrodynamic system, which reproduces the dynamics of fluctuations described by nearly incompressible magnetohydrodynamic in the plane perpendicular to a background magnetic field, is investigated by increasing the external forcing terms. Although this is the case closest to two-dimensional hydrodynamics, which shares some aspects with the classical Feigenbaum scenario of transition to chaos, the presence of magnetic fluctuations yields a very complex interesting route to chaos, characterized by the splitting into multiharmonic structures of the field amplitudes, and a mixing of phase-locking and free phase precession acting intermittently. When the background magnetic field lies in the plane, the system supports the presence of Alfvén waves thus lowering the nonlinear interactions. Interestingly enough, the dynamics critically depends on the angle between the direction of the magnetic field and the reference system of the wave vectors. Above a certain critical angle, independently from the external forcing, a breakdown of the phase locking appears, accompanied with a suppression of the chaotic dynamics, replaced by a simple periodic motion.

DOI: [10.1103/PhysRevE.104.025201](https://doi.org/10.1103/PhysRevE.104.025201)

### I. INTRODUCTION

Fluid flows forced by external perturbations may show complex emergent dynamics due to quadratic nonlinearities. The classical issue of the transition to chaos dates back to the 1960s [1,2], and some standard scenarios have been investigated through mathematical models, experimentally and numerically [3]. Truncated Galerkin models of two-dimensional (2D) incompressible hydrodynamic equations, obtained through a truncation to a finite (low) number of modes in the Fourier space, have been used [4]. If the number of modes is too small, their choice could result in altered phenomenology. The search for the minimal number of modes that stabilizes the dynamics, with respect to mode addition or substitution [4], provided uncertain results, presumably largely in excess [5,6], mainly because of the lack of universality of the Galerkin approximations [7]. Despite their sensitiveness to the mode selection, reduced models are able to capture with great detail features observed in experiments [8–14], providing insight on the macroscopic behavior at the

onset of turbulence [15–19]. In fact, one can recognize finite and/or infinite sequences of bifurcations [20,21], a quasiperiodic route to chaos [22,23], for low-dimensional chaos in a dissipation-dominated dynamical system, and a quasiperiodic route to intermittent chaos in a nearly conservative system [24]. In other words, a transition to a strange attractor behavior is observed through a series of quasiperiodic oscillations, which give rise to increasingly complicated attractors made of two very long intertwining periodic orbits.

In magnetohydrodynamic (MHD) flows, the charged fluid couples with the magnetic field, losing Galilean invariance and isotropy, supporting the presence of wavelike coupling, and in general introducing a greater complexity in the dynamics with respect to neutral fluids. In particular, the two-dimensional (2D) MHD case offers an interesting theoretical perspective. Large-scale fluctuations in interplanetary space plasmas present the typical statistical features of classical fully developed turbulence (e.g., Ref. [25] and references therein). Nearly incompressible MHD models [26,27] describe magnetofluids as being characterized by the superposition of 2D fluctuations, in a plane transverse to the background magnetic field, and slab fluctuations along the field. In this configuration, Alfvén waves are not present in

<sup>\*</sup>f.carbone@iia.cnr.it; francesco.carbone42@gmail.com

the 2D component of the fluctuations, so that the dynamics is controlled by the nonlinear time scale. Note that nearly incompressible MHD is highly relevant to solar wind fluctuations, where the 2D component corresponds to the majority of fluctuations observed by spacecraft [25–28]. This is remarkably similar to the 2D incompressible hydrodynamics case.

Since the pioneering work of Ruelle and Takens [2], the way chaotic orbits settle down to a chaotic attractor in a nonlinear system with quadratic nonlinearities (i.e., the turbulent flow behavior described by the Navier-Stokes equations), must be treated in the framework of a “dynamical systems approach” to turbulence [29]. While approximations have been used extensively for neutral fluids, the transition to turbulence in MHD flows has not been investigated in corresponding detail, with some exceptions concerning a nonchaotic, unforced, three-mode system [30,31]. Since MHD flows are described by a set of equations structurally similar to the Navier-Stokes system, it could be expected that the transition to chaos in magnetic turbulence follows the same route as its kinetic counterpart. Therefore, it is interesting to investigate whether or not the transition to turbulence mimics the route of neutral fluids. For example, if the background magnetic field, which cannot be eliminated by a Galilean transformation, has a component in the 2D plane, the dynamics is different from fluid flows. In this case, Alfvén waves can propagate linearly, and their characteristic propagation time competes with the nonlinear time, thus reducing the nonlinear interactions [32]. This perhaps may result in an alternate route to chaos, differentiating magnetized plasmas from neutral fluids.

Here, the chaotic behavior of a magnetofluid flow, and in particular the transition to chaos, has been investigated by using the simplest model for 2D MHD equations, i.e., a complex five-mode Galerkin approximation, extending existing models for neutral fluids [15–17] showing that the transition to chaos in a MHD system happens in an interesting way with respect to the fluid counterpart.

## II. A FIVE-MODE TRUNCATION OF TWO-DIMENSIONAL INCOMPRESSIBLE MHD

The incompressible MHD equations with a background magnetic field  $\mathbf{B}_0$  are written as:

$$\frac{\partial \mathbf{u}}{\partial t} - (\mathbf{c}_A \cdot \nabla) \mathbf{b} + (\mathbf{u} \cdot \nabla) \mathbf{u} - (\mathbf{b} \cdot \nabla) \mathbf{b} = -\nabla P_t + \nu \nabla^2 \mathbf{u} \quad (1)$$

$$\frac{\partial \mathbf{b}}{\partial t} - (\mathbf{c}_A \cdot \nabla) \mathbf{u} + (\mathbf{u} \cdot \nabla) \mathbf{b} - (\mathbf{b} \cdot \nabla) \mathbf{u} = \mu \nabla^2 \mathbf{b}, \quad (2)$$

with the conditions  $\nabla \cdot \mathbf{u} = 0$  and  $\nabla \cdot \mathbf{b} = 0$ . Here  $\mathbf{u}$  represents the velocity fluctuations,  $\mathbf{b} = (\mathbf{B} - \mathbf{B}_0)/\sqrt{4\pi\rho}$  the magnetic field Alfvénic fluctuations,  $\rho$  the constant mass density,  $P_t = P/\rho + b^2/2$  the total pressure,  $P$  the kinetic pressure, and  $\nu$ ,  $\mu$  the kinematic viscosity and resistivity respectively. The presence of the background magnetic field introduces the linear term proportional to the Alfvén speed  $\mathbf{c}_A = \mathbf{B}_0/\sqrt{4\pi\rho}$ . In two dimensions, the fields have only components  $\mathbf{u}(\mathbf{r}, t) = [u_x(x, y, t); u_y(x, y, t)]$ ,  $\mathbf{b}(\mathbf{r}, t) = [b_x(x, y, t); b_y(x, y, t)]$ , and evolve on a 2D torus  $0 \leq (x, y) \leq 2\pi$ .

In the wave-vector space, velocity and magnetic fluctuations can be defined in terms of Fourier coefficients as  $\mathbf{u}(\mathbf{r}, t) = \sum_{\mathbf{k}} \mathbf{u}(\mathbf{k}, t) e^{-i\mathbf{k} \cdot \mathbf{r}}$  and  $\mathbf{b}(\mathbf{r}, t) = \sum_{\mathbf{k}} \mathbf{b}(\mathbf{k}, t) e^{-i\mathbf{k} \cdot \mathbf{r}}$ , being  $\mathbf{k} = 2\pi \mathbf{n}/L$  and  $\mathbf{n} \in \mathbb{N}$  a pair of integers. Due to the divergence-free condition of the fields, Fourier coefficients can be written in terms of a unit polarization vector  $\mathbf{e}(\mathbf{k})$  perpendicular to the wave vector, say  $\mathbf{k} \cdot \mathbf{e}(\mathbf{k}) = 0$ , so that  $\mathbf{u}(\mathbf{k}, t) = u_{\mathbf{k}}(t) \mathbf{e}(\mathbf{k})$  and  $\mathbf{b}(\mathbf{k}, t) = b_{\mathbf{k}}(t) \mathbf{e}(\mathbf{k})$ . The unit vector must satisfy  $\mathbf{e}(\mathbf{k}) = \mathbf{e}^*(-\mathbf{k})$ , and  $\mathbf{e}(\mathbf{k}) \cdot \mathbf{e}^*(\mathbf{k}) = 1$ , so that it can be defined as  $\mathbf{e}(\mathbf{k}) = ik^{-1}(k_y, -k_x)$ ,  $k_x$  and  $k_y$  being the components of  $\mathbf{k}$  on the plane and  $k = |\mathbf{k}|$ . The MHD equations projected on the Fourier space become an infinite set of ordinary differential equations for the complex amplitudes:

$$\begin{aligned} \frac{du_{\mathbf{k}}(t)}{dt} - i(\mathbf{k} \cdot \mathbf{c}_A) b_{\mathbf{k}}(t) \\ = \frac{4\pi^2}{L^2} \sum_{\mathbf{p}, \mathbf{q}}^{\Delta} A_{\mathbf{k}\mathbf{p}\mathbf{q}}^+ [u_{\mathbf{p}}(t) u_{\mathbf{q}}(t) \\ - b_{\mathbf{p}}(t) b_{\mathbf{q}}(t)] - \nu k^2 u_{\mathbf{k}}(t) + R_{\mathbf{k}} \end{aligned} \quad (3)$$

$$\begin{aligned} \frac{db_{\mathbf{k}}(t)}{dt} - i(\mathbf{k} \cdot \mathbf{c}_A) u_{\mathbf{k}}(t) \\ = \frac{4\pi^2}{L^2} \sum_{\mathbf{p}, \mathbf{q}}^{\Delta} A_{\mathbf{k}\mathbf{p}\mathbf{q}}^- [b_{\mathbf{p}}(t) u_{\mathbf{q}}(t) \\ - u_{\mathbf{p}}(t) b_{\mathbf{q}}(t)] - \mu k^2 b_{\mathbf{k}}(t) + G_{\mathbf{k}}, \end{aligned} \quad (4)$$

where  $A_{\mathbf{k}\mathbf{p}\mathbf{q}}^{\pm} = 1/2[M_{\mathbf{k}\mathbf{p}\mathbf{q}} \pm M_{\mathbf{k}\mathbf{q}\mathbf{p}}]$  are the coupling coefficients of nonlinear terms, with  $M_{\mathbf{k}\mathbf{p}\mathbf{q}} = [-i\mathbf{k} \cdot \mathbf{e}(\mathbf{q})][\mathbf{e}^*(\mathbf{p}) \cdot \mathbf{e}(\mathbf{q})]$ . Finally, external forcing terms  $R_{\mathbf{k}}$  and  $G_{\mathbf{k}}$  have been introduced, which eventually act on the system, and the sum in the nonlinear term  $\sum_{\mathbf{p}, \mathbf{q}}^{\Delta} \equiv \sum_{\mathbf{p}, \mathbf{q}} \delta_{\mathbf{k}, \mathbf{p}+\mathbf{q}}$  is extended to all triads of wave vectors satisfying the triangular condition  $\mathbf{k} = \mathbf{p} + \mathbf{q}$ .

MHD can be alternatively described in terms of the linear Elsässer transformation [33]  $z_{\mathbf{k}}^{\pm}(t) = u_{\mathbf{k}}(t) \pm b_{\mathbf{k}}(t)$ , representing Alfvénic fluctuations propagating both in the direction of  $\mathbf{B}_0$  and opposite to it. The nonlinear MHD system (3) and (4) takes the more symmetric form [25,33–37]:

$$\begin{aligned} \frac{dz_{\mathbf{k}}^{\pm}(t)}{dt} \mp i(\mathbf{k} \cdot \mathbf{c}_A) z_{\mathbf{k}}^{\pm}(t) \\ = \frac{4\pi^2}{L^2} \sum_{\mathbf{p}, \mathbf{q}}^{\Delta} \sum_{\sigma = \pm 1} \Gamma_{\mathbf{k}\mathbf{p}\mathbf{q}}^{\sigma} z_{\mathbf{p}}^{\sigma}(t) z_{\mathbf{q}}^{-\sigma}(t) \\ - (k^2/2)[(\nu \pm \mu) z_{\mathbf{k}}^{+}(t) + (\nu \mp \mu) z_{\mathbf{k}}^{-}(t)], \end{aligned} \quad (5)$$

where  $\Gamma_{\mathbf{k}\mathbf{p}\mathbf{q}}^{\pm} = (A_{\mathbf{k}\mathbf{p}\mathbf{q}}^+ \pm A_{\mathbf{k}\mathbf{q}\mathbf{p}}^-)/4$  and  $F_{\mathbf{k}}^{\pm} = R_{\mathbf{k}} \pm G_{\mathbf{k}}$ . If  $\nu = \mu$ , the dissipative term becomes the usual  $-\nu k^2 z_{\mathbf{k}}^{\pm}$ . In the absence of forcing and dissipation, the number of wave vectors involved in the nonlinear couplings is infinite, and the system possesses three rugged invariants that survive each single triad of interacting wave vectors [31,38,39].

Since the rugged invariants survive every Galerkin truncation of the infinite system (5), a finite Lorenz-like low-order model  $\mathbb{L}_N(u, b)$ , which maintains all global characteristics of the complete system, can be obtained by taking into account only a finite sequence of  $N$  interacting modes  $\mathbf{k}_n$  ( $n =$

1, 2, ..., N), satisfying the triangular condition  $\mathbf{k}_n = \mathbf{k}_{n+r} \pm \mathbf{k}_{n+s}$  providing  $|n+r| \leq N$  and  $|n+s| \leq N$ , being  $(r, s) \in \mathbb{Z}$ .

Similarly to fluid turbulence [15,40], here a five-modes model  $\mathbb{L}_5(u, b)$  have been investigated by using the following wave vectors:  $\mathbf{k}_1 = (1, 1)$ ,  $\mathbf{k}_2 = (3, 0)$ ,  $\mathbf{k}_3 = (2, -1)$ ,  $\mathbf{k}_4 = (1, 2)$ , and  $\mathbf{k}_5 = (0, 1)$ , which satisfy the triangular relations  $\mathbf{k}_1 = \mathbf{k}_2 - \mathbf{k}_3 = \mathbf{k}_4 - \mathbf{k}_5$ ,  $\mathbf{k}_2 = \mathbf{k}_3 + \mathbf{k}_1$ ,  $\mathbf{k}_3 = \mathbf{k}_2 - \mathbf{k}_1$ ,  $\mathbf{k}_4 = \mathbf{k}_1 + \mathbf{k}_5$ , and  $\mathbf{k}_5 = \mathbf{k}_4 - \mathbf{k}_1$ . By explicitly calculating the coupling coefficients, and rescaling times by setting for simplicity  $\nu = \mu = 1$ , the MHD model can be written in dimensionless form as:

$$\begin{aligned} \dot{u}_1 &= 4(u_2 u_3^* - b_2 b_3^*) - 4(u_4 u_5^* - b_4 b_5^*) - 2u_1 + i\Omega_1 b_1 \\ \dot{u}_2 &= 3(u_3 u_1 - b_3 b_1) - 9u_2 + i\Omega_2 b_2 \\ \dot{u}_3 &= -7(u_2 u_1^* - b_2 b_1^*) - 5u_3 + i\Omega_3 b_3 + R \\ \dot{u}_4 &= (u_1 u_5 - b_1 b_5) - 5u_4 + i\Omega_4 b_4 \\ \dot{u}_5 &= 3(u_4 u_1^* - b_4 b_1^*) - u_5 + i\Omega_5 b_5 \\ \dot{b}_1 &= 2(b_2 u_3^* - u_2 b_3^*) - 2(b_4 u_5^* - u_4 b_5^*) - 2b_1 + i\Omega_1 u_1 \\ \dot{b}_2 &= 9(b_3 u_1 - u_3 b_1) - 9b_2 + i\Omega_2 u_2 \\ \dot{b}_3 &= -5(b_2 u_1^* - u_2 b_1^*) - 5b_3 + i\Omega_3 u_3 + G \\ \dot{b}_4 &= 5(b_1 u_5 - u_1 b_5) - 5b_4 + i\Omega_4 u_4 \\ \dot{b}_5 &= (b_4 u_1^* - u_4 b_1^*) - b_5 + i\Omega_5 u_5, \end{aligned} \quad (6)$$

where dotted variables represent time derivatives. The normalized fields are  $u_n(t) \equiv u_{\mathbf{k}_n}(t)/|\mathbf{c}_A| \in \mathbb{C}$  and  $b_n(t) \equiv b_{\mathbf{k}_n}(t)/|\mathbf{c}_A| \in \mathbb{C}$ , with the conditions  $u_{-n}(t) = u_n^*(t)$ ,  $b_{-n}(t) = b_n^*(t)$  and  $z_n^\pm(t) = (z_n^\pm)^*(t)$  on the complex conjugates. Here  $(\mathbf{k}_n \cdot \mathbf{e}_A) = \Omega_n$  is the Alfvén frequency ( $\mathbf{e}_A$  being the direction of the background magnetic field on the plane). Note that the linear term  $\Omega_n$  in Eq. (6) modifies the dynamics and the nonlinear coupling of the system by introducing the new timescale  $|\Omega_n|^{-1}$ , in addition to the dissipative and eddy-turnover times. The external parameters  $(R, G) \in \mathbb{C}$  are defined as  $R = R_i(1+i)$  and  $G = G_i(1+i)$  and act only on the mode  $n = 3$ , which will be hereafter named the kinetic and magnetic Reynolds numbers. We must impose  $G_i > 0$ , due to the antidynamo theorem [41], and  $G_i \neq R_i$ , thus preventing the collapse on the trivial maximum cross-helicity attractor  $u_n(t) = \pm b_n(t)$ , which stops the nonlinear interactions.

The set of equations describing the dynamics of the Elsässer variables can be immediately obtained from (6) by introducing the normalized variables  $z_n^\pm(t) \equiv z_{\mathbf{k}_n}^\pm(t)/|\mathbf{c}_A| \in \mathbb{C}$  and the external forcing terms  $F^\pm = (2/\sqrt{2})R_i^\pm \exp(i\pi/4)$  (being  $R_i^\pm = R_i \pm G_i$ ). In terms of amplitude and phase  $z_n^\pm(t) = Z_n^\pm(t) \exp[i\Phi_n^\pm(t)]$  the Elsässer MHD system becomes:

$$\begin{aligned} \dot{Z}_1^\pm &= \sum_{\sigma=\pm 1} (2+\sigma) Z_2^\sigma Z_3^{-\sigma} \cos \Delta_1^\sigma - 2Z_1^\pm \\ \dot{Z}_2^\pm &= \frac{3}{2} \sum_{\sigma=\pm 1} (1+3\sigma) Z_3^\sigma Z_1^{-\sigma} \cos \Delta_2^\sigma - 9Z_2^\pm \\ \dot{Z}_3^\pm &= -\frac{1}{2} \sum_{\sigma=\pm 1} (7+5\sigma) Z_2^\sigma Z_1^{-\sigma} \cos \Delta_3^\sigma - 5Z_3^\pm \\ &\quad + \frac{2}{\sqrt{2}} R_3^\pm \cos\left(\frac{\pi}{4} - \Phi_3^\pm\right) \end{aligned}$$

$$\begin{aligned} \dot{Z}_4^\pm &= \frac{1}{2} \sum_{\sigma=\pm 1} (1+5\sigma) Z_1^\sigma Z_5^{-\sigma} \cos \Delta_4^\sigma - 5Z_4^\pm \\ \dot{Z}_5^\pm &= \frac{1}{2} \sum_{\sigma=\pm 1} (3+\sigma) Z_4^\sigma Z_1^{-\sigma} \cos \Delta_5^\sigma - Z_5^\pm \\ \dot{\Phi}_1^\pm &= \frac{1}{Z_1^\pm} \sum_{\sigma=\pm 1} (2+\sigma) Z_2^\sigma Z_3^{-\sigma} \sin \Delta_1^\sigma \pm \sqrt{2} \cos \gamma_1 \\ \dot{\Phi}_2^\pm &= \frac{3}{2Z_2^\pm} \sum_{\sigma=\pm 1} (1+3\sigma) Z_3^\sigma Z_1^{-\sigma} \sin \Delta_2^\sigma \pm 3 \cos \gamma_2 \\ \dot{\Phi}_3^\pm &= -\frac{1}{2Z_3^\pm} \sum_{\sigma=\pm 1} (7+5\sigma) Z_2^\sigma Z_1^{-\sigma} \sin \Delta_3^\sigma \\ &\quad \pm \sqrt{5} \cos \gamma_3 + \frac{2}{\sqrt{2}} R_3^\pm \sin\left(\frac{\pi}{4} - \Phi_3^\pm\right) \\ \dot{\Phi}_4^\pm &= \frac{1}{2Z_4^\pm} \sum_{\sigma=\pm 1} (1+5\sigma) Z_1^\sigma Z_5^{-\sigma} \sin \Delta_4^\sigma \pm \sqrt{5} \cos \gamma_4 \\ \dot{\Phi}_5^\pm &= \frac{1}{2Z_5^\pm} \sum_{\sigma=\pm 1} (3+\sigma) Z_4^\sigma Z_1^{-\sigma} \sin \Delta_5^\sigma \pm \cos \gamma_5, \end{aligned} \quad (7)$$

where  $\gamma_n$  represents the angle between the wave vector  $\mathbf{k}_n$  of the  $n$ th mode and the direction  $\mathbf{e}_A$  of the background magnetic field. The triad-phase relations are defined as  $\Delta_1^\sigma = \Phi_2^\sigma - \Phi_3^{-\sigma} - \Phi_1^\sigma$ ,  $\Delta_2^\sigma = \Phi_3^\sigma + \Phi_1^{-\sigma} - \Phi_2^\sigma$ ,  $\Delta_3^\sigma = \Phi_2^\sigma - \Phi_1^{-\sigma} - \Phi_3^\sigma$ ,  $\Delta_4^\sigma = \Phi_1^\sigma + \Phi_5^{-\sigma} - \Phi_4^\sigma$  and  $\Delta_5^\sigma = \Phi_4^\sigma - \Phi_1^\sigma - \Phi_5^\sigma$ . The background magnetic field is responsible for a phase shift of the Elsässer modes, while the dissipation affects only the amplitudes.

Trivial stationary states of the system are described by  $Z_n^\pm = 0$  and  $\Phi_n^\pm(t) = \Phi_n^\pm(0)$ , for all modes, but  $Z_3^\pm = (\mp 2R^\pm/5\sqrt{2}) \cos(\cot^{-1} \Omega_3)$ ,  $\Phi_3^\pm = \pi/4 \pm \cot^{-1} \Omega_3$ . For the purely kinetic system where  $u_n = U_n \exp(i\Phi_n)$ , the trivial stationary state is  $U_3 = 2R/5\sqrt{2}$ ,  $\Phi_3 = \pi/4$  ( $U_3 = R/5$  for the real kinetic system), while in absence of the background magnetic field, the stationary states are  $Z_3^\pm = \mp 2R^\pm/5\sqrt{2}$ ,  $\Phi_3^\pm = \pi/4$ .

The system of equations (6) has been numerically integrated with an explicit Runge-Kutta-Dormand-Prince method [42,43], with the error tolerance set at  $10^{-8}$ . The three invariants of the inviscid and unforced system are conserved within the error tolerance. Each run is initialized with the same initial condition: Eqs. (6) have been evolved for a total time  $t = 550$ , with  $R_i = 15$  for the kinetic case, and  $R_i = 20$  and  $G_i = 30$  for the MHD case, both resulting in a stable stationary solution.

### III. PURELY KINETIC SYSTEM

The kinetic system  $\mathbb{L}_5(u, 0)$  has been initially investigated, using the complex variables  $u_n(t) \in \mathbb{C}$  and setting  $b_n(t) = 0$ . The real kinetic case has been previously investigated [15,20]. The left panel of Fig. 1 shows the bifurcation diagram obtained from the mode  $|u_1(t)|^2$  of the system (3) as the forcing  $R_i$  varies in the range  $R_i \in [15, 25]$ . Each point corresponds to a local maximum of the kinetic energy of the mode. Modes with  $n > 1$  display the same bifurcation diagram, with different amplitudes. For very weak forcing (not shown) the system has a trivial fixed point, which is destabilized, as  $R_i$  increases,

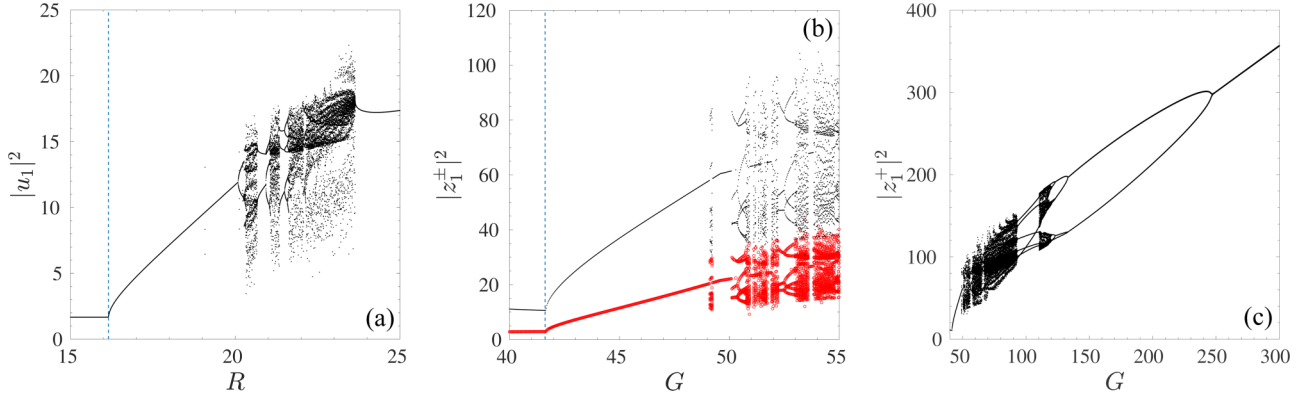


FIG. 1. Left: Bifurcation diagram of the mode  $|u_1|^2$  for a neutral fluid for  $R_i \in [15, 25]$ . The vertical dashed line indicates the Hopf bifurcation. Middle: Bifurcation diagram of the Elsässer variables  $|z_1^+|$  (black dots) and  $|z_1^-|$  (red circles), for magnetic forcing  $G_i \in [40, 55]$ . The vertical dashed line indicates the Hopf bifurcation. Right: Bifurcation diagram of the Elsässer variable  $|z_1^+|$  for a wider range of magnetic forcing  $G_i \in [50, 300]$ .

through a pitchfork bifurcation, thus obtaining a steady state  $u_n \neq 0 \forall n$ . At the threshold  $R_1^* \simeq 16.15$ , the system undergoes a Hopf bifurcation, reaching oscillating periodic solutions for  $16.15 \leq R_i < 20.32$ . In the range  $20.32 \leq R_i \leq 23.645$ , the system enters in a complex chaotic region of alternation between strong turbulence and periodicity windows, characterized by the presence of multiple strange attractors [20].

At  $R_2^* \simeq 20.07$  the amplitude  $|u_1(t)|^2$  presents a periodic modulation, and the autocorrelation function  $C_1(\ell)$  shows a sequence of maxima at lag times  $\ell/T_0^k = j$ , where  $j = 1, 2, \dots$ , and  $T_0^k = 0.815$ . The transition to chaotic dynamics is obtained through a sequence of successive bifurcations characterized by period doubling. The first one, as shown in Fig. 2, occurs at  $R_3^* \simeq 20.25$ . The appearance of subharmonics is observed in the autocorrelation function with maxima at lag times  $\ell/T_0^k = 2$ . A second bifurcation is observed at  $R_4^* = 20.29$  with maxima of the autocorrelation function at about  $\ell/T_0^k = 4$ . The sequence is compatible with the Feigenbaum conjecture [44], characterized by a fixed ratio for the various bifurcation points  $\delta \equiv \lim_{i \rightarrow \infty} \frac{R_i^* - R_{i-1}^*}{R_{i+1}^* - R_i^*}$ , being  $R_i^*$  the forcing at the  $i$ th bifurcation point (see Table I). The value of the Feigenbaum constant evaluated for those points is  $\delta_{2,3,4} \simeq 4.64$ , consistent with the expected parameter  $\delta_\infty \simeq 4.6692 \dots$  [44].

The structure of this sequence of bifurcations is consistent with previous studies for real variables [15,20]. The main

difference between the real and complex cases is related to the different bifurcation values. Here, the bifurcation sequence is observed at lower  $R_i^*$ , due to complex forcing responsible for injecting higher amount of energy in the system. Finally, the turbulence is suppressed in favor of a second quiescent region, where the strange attractor shrinks to a stable periodic orbit for  $R_i \geq 23.645$ .

#### IV. DYNAMICAL MHD BEHAVIOR IN THE ABSENCE OF BACKGROUND MAGNETIC FIELD

This is the closest MHD case to hydrodynamics, corresponding to a magnetofluid with an external field perpendicular to the fluctuations plane, as described by nearly incompressible MHD [26]. Let us consider the complex truncated MHD system  $\mathbb{L}_5(u, b)$  with  $\Omega_n = 0$ . The kinetic Reynolds number has been fixed at  $R_i = 20$  (periodic solution), while the magnetic Reynolds number is varied in the range  $G_i \in [40, 400]$ . As a general feature, when the magnetic field is switched on, the dynamics of the system becomes richer, and the transition to turbulence is observed via a slightly different mechanism. It should be remarked that the fine structure and the richness of the various dynamical regimes, emerging as  $G_i$  is varied, cannot be described concisely. Therefore, by using Elsässer variables, we report

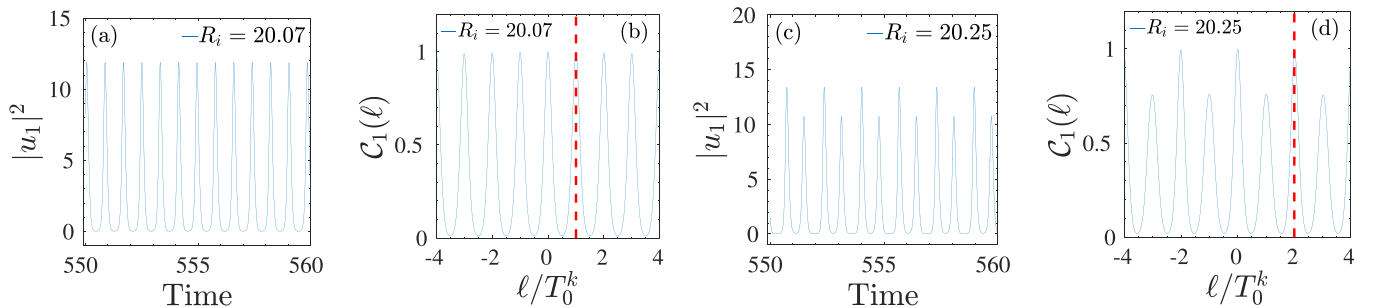


FIG. 2. Temporal evolution of the mode  $|u_1(t)|^2$  for the purely kinetic system, at  $R_i = 20.07$  and  $R_i = 20.25$ , and the associated autocorrelation functions  $C_1(\ell)$ . The vertical dashed lines indicates the maximum of the autocorrelation function corresponding to a time lag multiple of the characteristic period  $T_0^k \equiv 0.815$ , compatible with  $\ell/T_0^k = 1$  and  $\ell/T_0^k = 2$ .

TABLE I. Kinetic Reynolds values associated to the first four bifurcation points observed for a pure kinetic evolution of Eq. (6).

$i$ th Bifurcation point	$R_i^*$
1	16.15
2	20.07
3	20.25
4	20.29

in the following only the main features of the transition to turbulence.

### A. Bifurcation analysis at low-forcing regimes

The central panel of Fig. 1 depicts the bifurcation diagram of the Elsässer pseudoenergies of the mode  $|z_1^\pm|^2$ , in the range  $G_i \in [40, 55]$ . For very small forcing  $G_i$  (not shown here), the trivial fixed point is destabilized through a pitchfork bifurcation leading to the stationary steady state  $z_n^\pm = \text{const.} \neq 0 \forall n$ . This is in turn destabilized through an Hopf bifurcation at  $G_i^* \simeq 41.62$ , visible in both Elsässer pseudoenergies of all modes  $|z_n^\pm|^2$ . For stronger forcing, the system has an attracting closed orbit, similar to the kinetic case [15]. At  $G_i \simeq 49.12$  the periodic orbit loses stability, generating structures characterized by different values of maximum pseudoenergies, which split as  $G_i$  is increased. This phase is followed by an abrupt shrinking to a new periodic orbit as the forcing approaches  $G_i \sim 49.24$ . An example is shown in the top panels of Fig. 3, depicting the numerical solution of the system projected onto the plane  $(|z_1^+|^2; |z_3^+|^2)$  for different values of the magnetic

forcing  $G_i$ . Starting from a periodic oscillation (top-left panel) at  $G_i = 49.10$ , the increment of the magnetic forcing destabilizes the periodic motion, accompanied by the splitting of the orbits. This continues (with number of out-coming secondary orbits changing with the forcing) for successive increments of  $G_i$  (second and third panel), until the dynamics closes again around a single steady state at  $G_i = 49.24$  (top-right panel).

The characteristic oscillation period, observed at  $G_i = 49.10$ , is shorter than for the kinetic case:  $T_0^m \approx 0.563$ , the maxima of the autocorrelation function being characterized by time intervals of about  $\ell/T_0^m = 1$ . At  $G_i = 49.18$  a first bifurcation is observed, the autocorrelation function  $C_1(\ell)$  presents a complicated structure with multiple peaks at different lags  $\ell$ , as shown in the bottom panels of Fig. 3. Four local maxima of different amplitude are present in the autocorrelation function, compatible with lag times  $\ell/T_0^m = 1, 3.79, 4.76, 5.7$ . At variance with the kinetic case, in MHD the transition to chaos does not take place through a sequence of period doublings, but rather through the abrupt appearance of subharmonic structures, evidenced again at higher  $G_i$ , and for real forcing  $G \in \mathbb{R}$ .

Using a different approach, the absence of period doubling is also evidenced by the Poincaré-like return map  $P_1^{(n+1)} = f[P_1^{(n)}]$ , where  $P_1^{(n)} = \text{Max}|z_1^\pm|^2$  is the  $n$ th maximum of  $|z_1^\pm|^2$  [45], shown in the left panel of Fig. 4 for different  $G_i$ . The map spreads as  $G_i$  increases. At  $G_i = 49.10$ , the map (blue circle) consists of one single point, indicating a periodic solution with identical amplitude (shown for  $|z_1^+|^2$  in the first panel of Fig. 5). As the forcing increases, the orbit splitting appears ( $G_i = 49.15$ ), and the map (red squares) consists of ten points, corresponding to symmetric repetitions of two clusters of

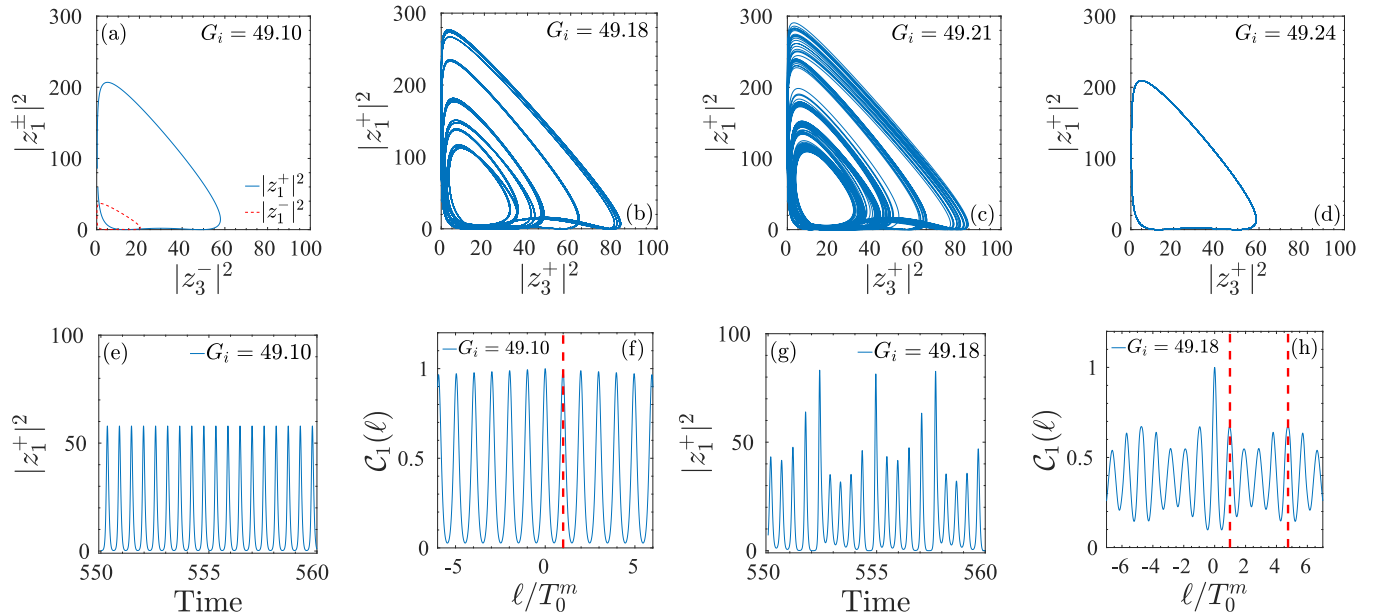


FIG. 3. First row: Evolution of the phase space trajectory, projected on the plane  $|z_1^+|^2, |z_3^+|^2$ , at different forcing  $G_i$ . The dynamics evolves through the opening of multiple quasiperiodic oscillations, characterized by multiple orbits, which close on a successive periodic solution. The phase space have been constructed by iterating the solutions in the range of times  $t \in [550, 650]$ . Second row: Temporal evolution and autocorrelation functions of the MHD mode  $|z_1^+|^2$  for  $G_i = 49.10$ , before the bifurcation, and  $G_i = 49.18$ , after the bifurcation. For  $G_i = 49.18$  multiple maxima with comparable amplitude are observed. The vertical dashed line indicates the maximum of the autocorrelation function corresponding to a time lag multiple of the characteristic period  $T_0^m \approx 0.563$ , compatible with  $\ell/T_0^m = 1$  and  $\ell/T_0^m = 4.76$  ( $4.76 \times T_0^m \approx 2.68$ ).

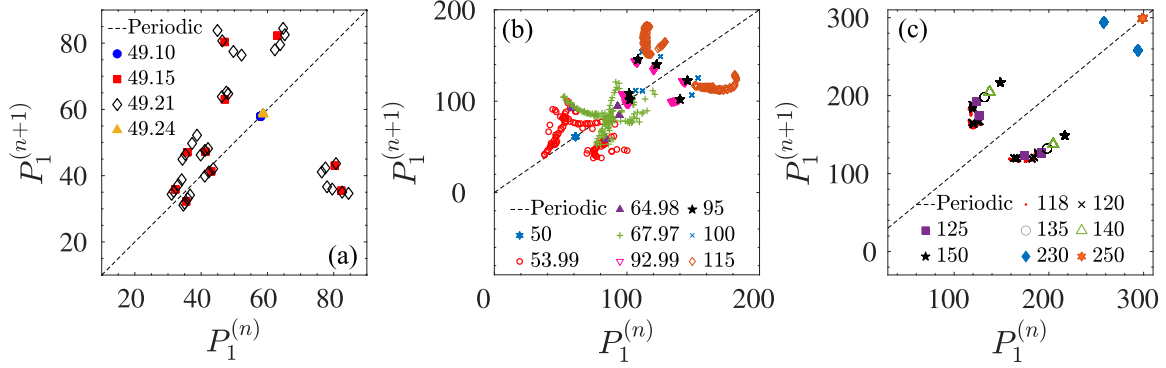


FIG. 4. Left: Poincaré return maps as a function of the magnetic Reynolds number  $G_i$  for  $|z_1^\pm|^2$ , showing the transition from periodic (circles) to multiperiodic solution (squares), to the spreading around the previous map positions (diamonds), and eventually to the second single point (periodic) with different amplitude and period (triangles). Middle: Poincaré return maps for  $|z_1^\pm|^2$  in the turbulent region, for different magnetic forcing  $G_i \in [50, 115]$  (see legend for color coding). Right: Poincaré return maps for  $|z_1^\pm|^2$  depicting the coalescence from the two-lobe attractor ( $G_i = 118$ ) to a periodic motion ( $G_i = 250$ ), for different magnetic forcing  $G_i \in [118, 250]$  (see legend for color coding).

five increasing peaks (regions *I* and *II* in the second panel of Fig. 5). For larger forcing, each of the ten points in the map spreads into four points (open diamonds), indicating a superposed amplitude modulation of the peaks with time. The same behavior is observed in all modes for both Elsässer components.

**B. Transition to turbulence and return to periodicity at high-forcing regimes**

As the magnetic forcing approaches  $G_i \simeq 51$ , a sudden transition to a fully turbulent state is observed (middle and right panels of Fig. 1), resulting in a strange attractor in the phase space. The transition was also observed in the power spectral density of the temporal dynamics, changing from discrete to broad band [3,46,47]. An example of  $|z_1^\pm|^2(t)$  is shown in the third panel of Fig. 5 for  $G_i = 60$ , where the clustered peaks observed for smaller  $G_i$  disappear in favor of a complex, nonperiodic dynamics, evidencing the onset turbulent regime.

Starting from the periodic solution, as the forcing increases, the turbulent return maps evolve accordingly (Fig. 4, right panel). When periodic solutions are observed, the map consists of one point ( $G_i = 50$ , blue six-pointed star), while during the transition to turbulence the phase space becomes

intermittently covered by complex structures spread over the plane. At  $G_i = 53.99$  (red empty circles), the Poincaré map shows the cusps typical of the Lorenz map [1,48]. The corresponding strange attractor is shown in the first panel of Fig. 6. As the forcing increases ( $G_i = 64.98$ ), the strange attractor disappears, and a quasiperiodic orbit arises, highlighted in the map by four clustered points (violet up-pointing triangle) indicating subharmonic peaks with multiple orbits in the phase plane. At  $G_i = 67.97$  the orbits become unstable again forming a map densely distributed on a sequence winding around the bisector (green crosses), indicating transition to a new strange attractor. At  $G_i = 92.99$  (purple down-pointing triangle) the attractor tends to disappear again, as the system is approaching a wide subharmonic window with at least six orbits, starting at  $G_i \approx 95$  (black stars) and extending up to  $G_i = 100$  (blue  $\times$  symbol). The transition through the subharmonic window is depicted in the third panel of Fig. 6, showing the phase-space behavior for three different forcing  $G_i$ .

A small turbulent patch is observed for  $G_i \in [110, 118]$  (brown diamonds in the right panel of Fig. 4 at  $G_i = 115$ , see also the third panel of Fig. 6). At larger forcing, the map consists of two distinct dense wings, indicating a gradual structural evolution of the phase-space to a two-lobes attractor. In the final stage of evolution, a sequence of secondary clos-

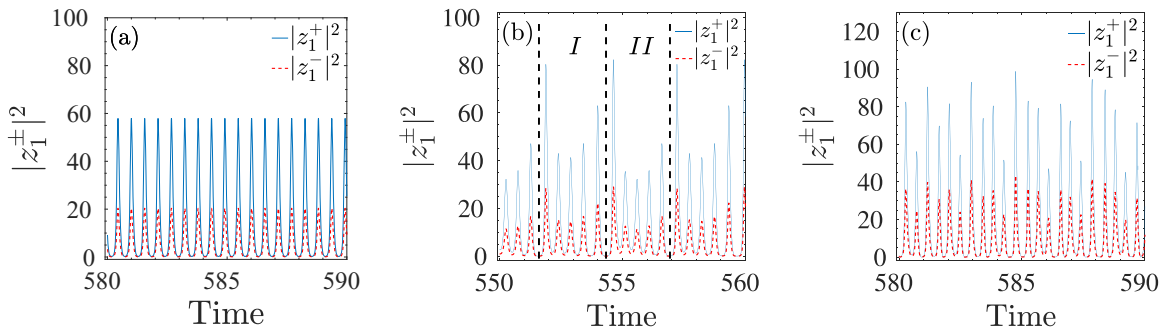


FIG. 5. Left: Temporal evolution of  $|z_1^+|^2$  and  $|z_1^-|^2$  in the periodic case at  $G_i = 49.10$ . Middle: An example of the alternation of clusters *I* and *II*, observed for  $G_i = 49.15$ . Each cluster is composed of five peaks with different amplitudes. The dashed lines separate the two clusters. Right: Temporal evolution of  $|z_1^+|^2$  and  $|z_1^-|^2$  in the turbulent state at  $G_i = 60$ .

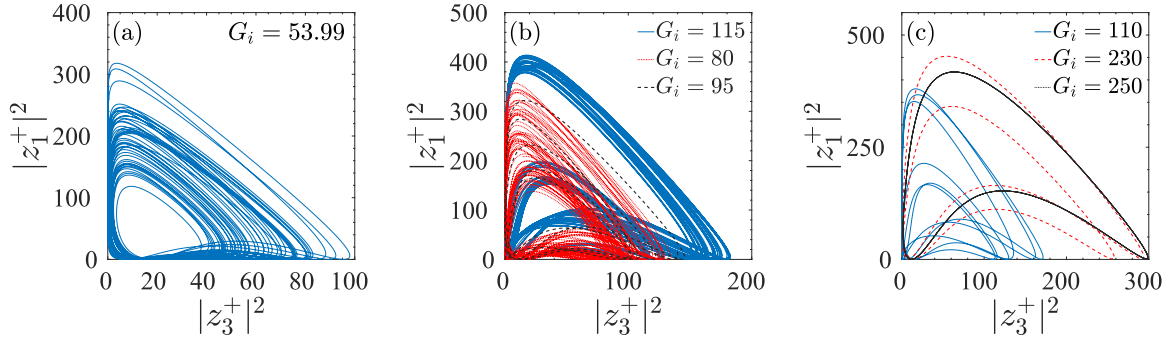


FIG. 6. Left: The strange attractor in the phase space  $|z_1^+|^2 - |z_3^+|^2$  for turbulent dynamics at  $G_i = 53.99$ . Middle: Same as previous panel for three larger forcing values (see legend). Shrinking and reopening of multiple orbits is observed near the largest periodicity window. Right: Same as previous panel for three larger forcing values (see legend). Coalescence of multiple orbits on a periodic motion is visible.

ing bifurcations shrinks the map to chaotic or subharmonic orbits. As shown in the bifurcation diagram (Fig. 1, middle and right panels), for  $G_i > 118$  the turbulent dynamics is completely suppressed in favor of multiple stable subharmonic orbits [49]. These gradually merge to a single periodic motion [49–52], with period  $T_0^m \simeq 0.17$ , reached for  $G_i \approx 240$ . The coalescence of multiple orbits is shown in the right panel of Fig. 6. Starting from the turbulent regime at  $G_i = 110$ , the phase space presents a transition to a two-lobe attractor ( $G_i = 230$ ), and gradually to periodic motion ( $G_i = 250$ ). The Poincaré return map depicting the coalescence to a single periodic orbit, is reported in the last panel of Fig. 4.

### C. Phase dynamics and phase transition curve

Additional interesting information on the system is provided by the temporal evolution of the phases  $\Phi_n(t)^\pm$ . Their

dynamics can be described through a phase transition curve (PTC) [53–55] by mapping the phases at two different times  $t_m$  and  $t_{m+1}$  as  $\Phi_n^\pm(t_{m+1}) = [\Phi_n^\pm(t_m) + w_n(G)] \bmod (2\pi)$ , separated by a phase shift  $w_n(G)$ , which depends on the magnetic forcing. The PTC is thus the analog for phases of the Poincaré map.

At small  $G_i$ , when the dynamics is periodic, all modes have constant phase, i.e.,  $w_n(G) = 0$  (top left panel of Fig. 7), which satisfies the phase-triad conditions  $\Delta_n^\pm = 0$ , except for mode  $n = 3$ , where the fixed point  $\Phi_3^\pm(t) = \pi/4$  is induced by the external forcing. The PTC consists of one point on the plane  $(\Phi_n^\pm(t_m); \Phi_n^\pm(t_{m+1}))$  (red square in the first panel of Fig. 8).

As  $G_i$  increases, the phase-triad condition is destabilized. When subharmonic structures arise ( $G_i = 49.15$ ), a periodic phase shift, represented as a phase precession on two different angles, is observed for all Elsässer modes  $z_n^\pm(t)$ . The PTC

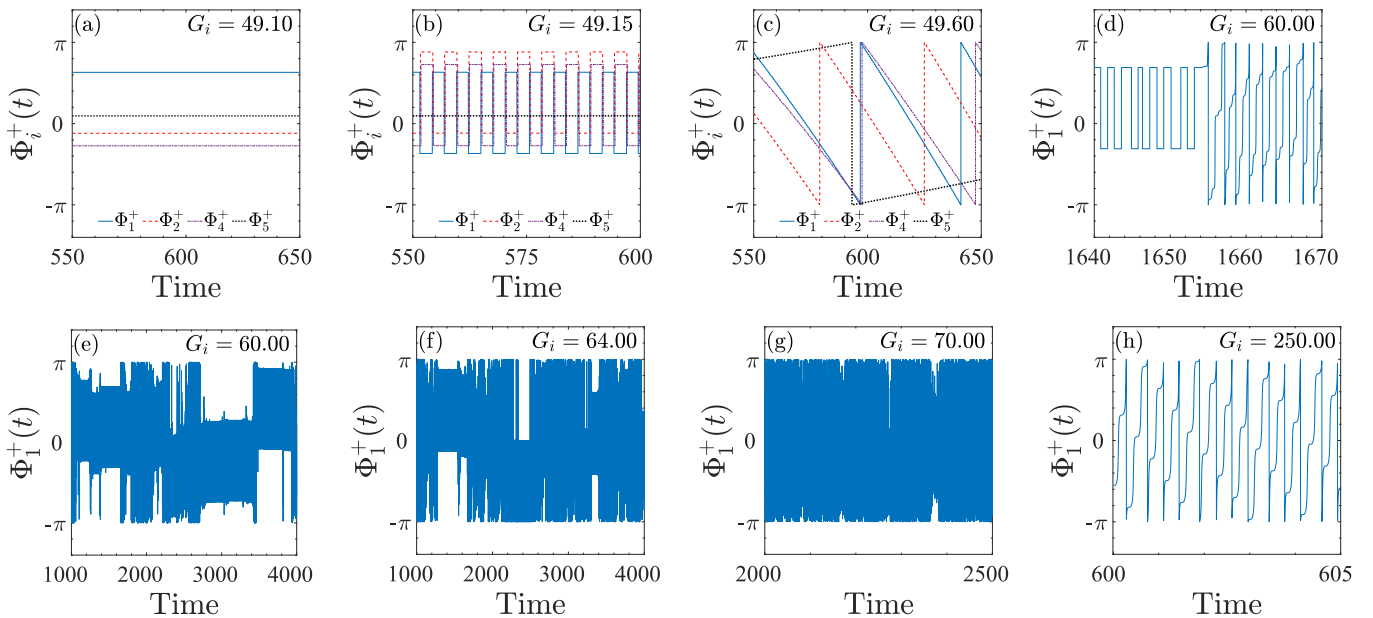


FIG. 7. Top: Temporal evolution of the phases  $\Phi_n^+(t)$  with  $n = 1, 2, 4, 5$ , for four distinct forcing values, depicting the route: locked phases (a), piece-wise constant phase (b), free precession (c), and mixed regime showing the superposition of piece-wise locked period and free precession (d). Bottom panels: temporal evolution of  $\Phi_1^+(t)$  for  $G_i = 60$  (e),  $G_i = 64$  (f), and  $G_i = 70$  (g). The reduction of the phase-locking intervals in favor of free precession intervals is visible by varying the forcing  $G_i$ . At larger forcing e.g.  $G_i = 250$  (h), the piece-wise phase locking is lost.

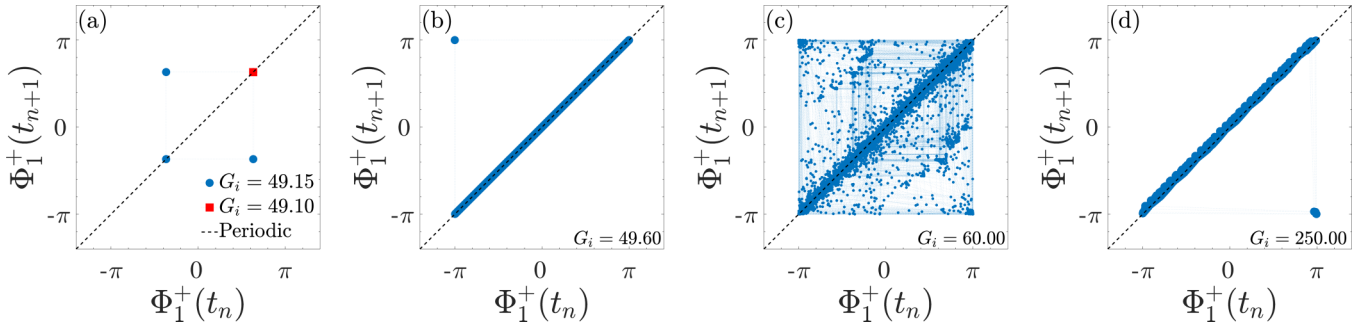


FIG. 8. Left: PTC for  $G_i = 49.09$  and  $G_i = 49.15$ , showing the transition from a single-point map (red squares) to a four-point map (blue circles). Second panel: PTC for  $G_i = 49.60$ , describing the continuous time varying phase (all points on the line) and the periodic rotation of  $2\pi$  (the single point in the top-left corner). Third panel: PTC for  $G_i = 60.00$ , corresponding to the mixed regime. The square structures of the piecewise constant phase (cf. left panel) is highlighted by connecting lines. Right: PTC for  $G_i = 250$ , outside of the turbulent region. All the points lie around the central line, and one cluster is present in the bottom-right corner. Connecting lines highlight the structure of the map.

map shows four points, two on the bisector and two at opposite angles (first panel of Fig. 8, blue circles). In terms of temporal evolution, the phases are constant for a given time  $t_0$ , then switch to a different value, resulting in step function of piecewise locked phases (Fig. 7 first row, second panel). The phase shift terms in the PTC are then a sequence of periodic  $\delta$  functions  $w_n(G) = \pm w_0^{(n)} \delta(t_m - t_0)$ , where the  $\delta$  function changes the sign of  $w_n(G)$  every  $t_0$ , generating the precession, and  $w_0^{(n)}$  is a constant for each mode. The term  $w_n(G)$  is responsible for the points outside the bisector. As an exception, the phase of the smallest wave vector  $\mathbf{k}_5$  remains stable up to larger forcing, even satisfying the phase-triad relation  $\Phi_5^\pm = \Phi_4^\pm - \Phi_1^\mp$ .

As  $G_i$  further increases the locked phase structure is destroyed and phase precession occurs in the dynamics. In this regime the phase shifts, depending linearly on time (Fig. 7 first row, third panel), and all the points densely cover a line at a fixed distance from the bisector of the PTC (second panel of Fig. 8). In this case  $w_n(G) = \pm \alpha_n$  is constant for each mode, whose sign is related to the precession direction. For the large-scale mode  $\Phi_5^\pm$ , the constant phase shift is much slower than the other modes.

Interestingly, the transition to the turbulent regime at  $G_i \simeq 60$ , is characterized by a phase dynamic, which presents a mixed behavior, namely the superposition of random periods of piecewise locked phases, alternating to periods of free precession. The temporal evolution of the phase  $\Phi_1(t)^+$  in this turbulent regime can be seen in the top-right and bottom-left panels of Fig. 7. A weak modulation is always visible in all time-varying regions of  $\Phi_n(t)^\pm$ , indicating very short periods of braked precession. The PTC, shown in the third panel of Fig. 8, presents multiple features, namely: (i) clusters of points at the vertices of the square structure of each piecewise region; (ii) a dense cloud of points scattered around the bisector, indicating random precession angle (as in the time-dependent case); and (iii) two smaller clouds of points at the top-left and bottom-right corners of the map, indicating that the phase rotate both clockwise and counterclockwise.

The mixed regime persists up to  $G_i \simeq 70$ , where the transition is characterized by a continuous shrinking of phase-locked periods as  $G_i$  increases (Fig. 7 first bottom three panels). When the periods of phase-locking disappear, the

dynamics is characterized by a continuously time-varying phase with an unidirectional random angle of rotation for each mode. The weak modulation of very short period of braked precession is always present. This regime of phases is finally stable up to higher forcing values (e.g.,  $G_i = 250$ , last panel of Figs. 7 and 8, respectively), thus persisting even when the turbulent regime is suppressed.

## V. DYNAMICAL MHD BEHAVIOR IN THE PRESENCE OF BACKGROUND MAGNETIC FIELD

When a background magnetic field  $\mathbf{B}_0$  is present in the plane, the symmetry on the  $(x, y)$  plane is lost by the introduction of the privileged direction  $\mathbf{e}_A$ , making the system anisotropic. Moreover, the linear term introduces a further characteristic time scale  $|\Omega_n|^{-1}$  due to Alfvén waves propagating along the background magnetic field, which can compete with the eddy-turnover time [27]. In this configuration, the MHD case is thus substantially different from the hydrodynamic case. The linear terms  $\Omega_n(\theta)$  of the MHD system depend on the angle  $\theta$  between  $\mathbf{e}_A$  and the  $x$  axis. As shown in Sec. II, the ambient field affects the phases  $\Phi_n^\pm(t)$  through a factor proportional to  $\Omega_n$ , so that the dynamics becomes strongly dependent on  $\theta$ . Such dependence is described in Fig. 9 where we show the bifurcation diagram for different values of the angle  $\theta$ .

As in the previous cases, the trivial stationary state is at first destabilized through a pitchfork bifurcation, leading to the steady state with constant  $u_n$  and  $b_n$ , which is further destabilized through a Hopf bifurcation as  $G_i$  increases. The bifurcation point  $G_i$  is higher as  $\theta$  increases. Similarly, the intermittent subharmonics also emerge at different values of the forcing (Fig. 9). For  $\theta = 15^\circ$ , intermittent structures form at  $G_i \simeq 80$ ; for  $\theta = 30^\circ$  two sets of structure are formed, at  $G_i \simeq 60$  and  $G_i \simeq 110$ ; for  $\theta = 60^\circ$   $G_i \simeq 120$  and  $G_i \simeq 130$ ; for  $\theta = 75^\circ$   $G_i \simeq 250$ . Independent of the angle, secondary bifurcations will occur in the first stage of the evolution. Even in this case, secondary bifurcations do not follow the Feigenbaum pattern. The transition to chaos occurs at values of  $G_i$  larger than in absence of the background field, and the turbulent region in the bifurcation diagram (in terms of forcing range) is stretched, showing the maximum extension in a range of angles  $\theta \in [30^\circ, 60^\circ]$  (Fig. 9).

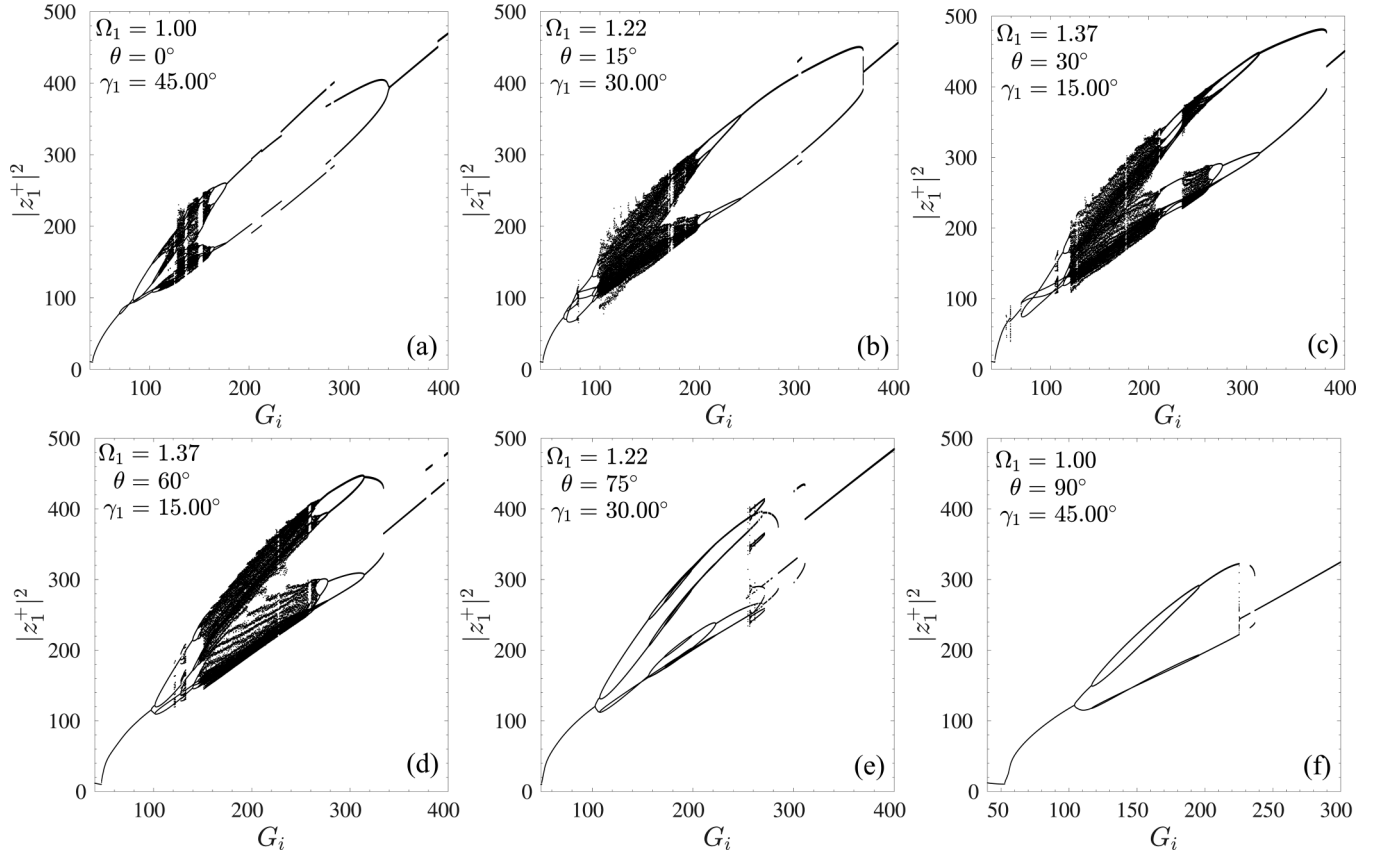


FIG. 9. From top-left to bottom-right: For the system with ambient field, bifurcation diagrams of  $|z_1^+(t)|^2$  as a function of the forcing  $G_i \in [50, 400]$ , at six different angles  $\theta$  (see panel titles). The corresponding Alfvénic timescale  $\Omega_n$  and the angle  $\gamma_n$  between  $\mathbf{k}_n$  and  $\mathbf{e}_A$  are also indicated.

A different dynamics emerge when the angle exceeds  $\theta = 60^\circ$ . In this case, the turbulent region begins to shrink, and disappears above a defined angle  $\bar{\theta}$ , where only subharmonic or periodic structures are present (Fig. 9 second row). This peculiar feature could be related to the presence of two competing phenomena in MHD, related to two characteristic timescales, i.e., the eddy-turnover time [56] defined as  $\tau_{nl} \sim (k_n \sqrt{k_n E_n})^{-1}$ , being  $E_n = 1/2 \int (|z_n^+ + z_n^-|^2 + |z_n^+ - z_n^-|^2) dt$  and the sweeping time due to the propagation of Alfvén waves  $|\Omega_n|^{-1}$ . Table II collects both characteristic times at different angles  $0 \leq \theta \leq 90^\circ$ . For  $\theta < \bar{\theta}$ , the nonlinear evolution is always more efficient than the sweeping of fluctuations due to waves, since  $\tau_{nl} < |\Omega_n|^{-1}$  for all modes. On the other hand, when the angle exceed the value  $\tan \bar{\theta} = 2$  ( $\bar{\theta} \simeq 63.4^\circ$ )  $|\Omega_3|^{-1}$

becomes negative, contrasting the onset of turbulence, while it stays positive for the other modes. In such a situation the two temporal scales compete in driving the dynamics.

The energy injected in the system is then not efficiently transferred to all modes, because the sweeping effects, acting between opposite Elsässer fluctuations, are enforced by the Alfvénic transport. As a result, when  $\theta$  increases, the presence of MHD waves strongly stabilizes the dynamics, with a transition from a chaotic regime ( $\theta \leq \bar{\theta}$ , as  $\theta$  increase the turbulent region appears at higher forcing values as reported in Fig. 9, top panels) to a quasiperiodic or periodic regime ( $\theta > \bar{\theta}$ ) regardless of forcing amplitude [32,57–59]. This is particularly evident for  $\theta \geq 70^\circ$  (two bottom-right panels of Fig. 9), since the Elsässer mode amplitudes are smooth in

TABLE II. Comparison of the characteristic nonlinear timescale  $\tau_{nl}$  and the decorrelation timescale  $\Omega_n^{-1}$  at different angle  $\theta$  of the ambient magnetic field  $\mathbf{B}_0$ . The nonlinear timescales have been obtained by setting  $\nu = \mu = 0$ ,  $R_i = G_i = 0$ .

nth mode	$k_n$	$\theta = 0^\circ$		$\theta = 30^\circ$		$\theta = 45^\circ$		$\theta = 60^\circ$		$\theta = 65^\circ$		$\theta = 70^\circ$		$\theta = 90^\circ$	
		$\tau_{nl}$	$\Omega_n^{-1}$	$\tau_{nl}$	$\Omega_n^{-1}$	$\tau_{nl}$	$\Omega_n^{-1}$	$\tau_{nl}$	$\Omega_n^{-1}$	$\tau_{nl}$	$\Omega_n^{-1}$	$\tau_{nl}$	$\Omega_n^{-1}$	$\tau_{nl}$	$\Omega_n^{-1}$
1	$\sqrt{2}$	0.255	1	0.269	0.732	0.275	0.707	0.261	0.732	0.287	0.753	0.261	0.780	0.251	1
2	3	0.089	1/3	0.086	0.385	0.086	0.471	0.088	2/3	0.077	0.789	0.091	0.975	0.107	$\infty$
3	$\sqrt{5}$	0.136	1/2	0.133	0.812	0.133	1.414	0.132	7.464	0.121	-16.374	0.139	-3.911	0.160	-1
4	$\sqrt{5}$	0.141	1	0.132	0.536	0.143	0.471	0.132	0.448	0.142	0.447	0.132	0.450	0.123	1/2
5	1	0.424	$\infty$	0.449	2	0.412	1.414	0.460	1.155	0.510	1.103	0.424	1.064	0.384	1

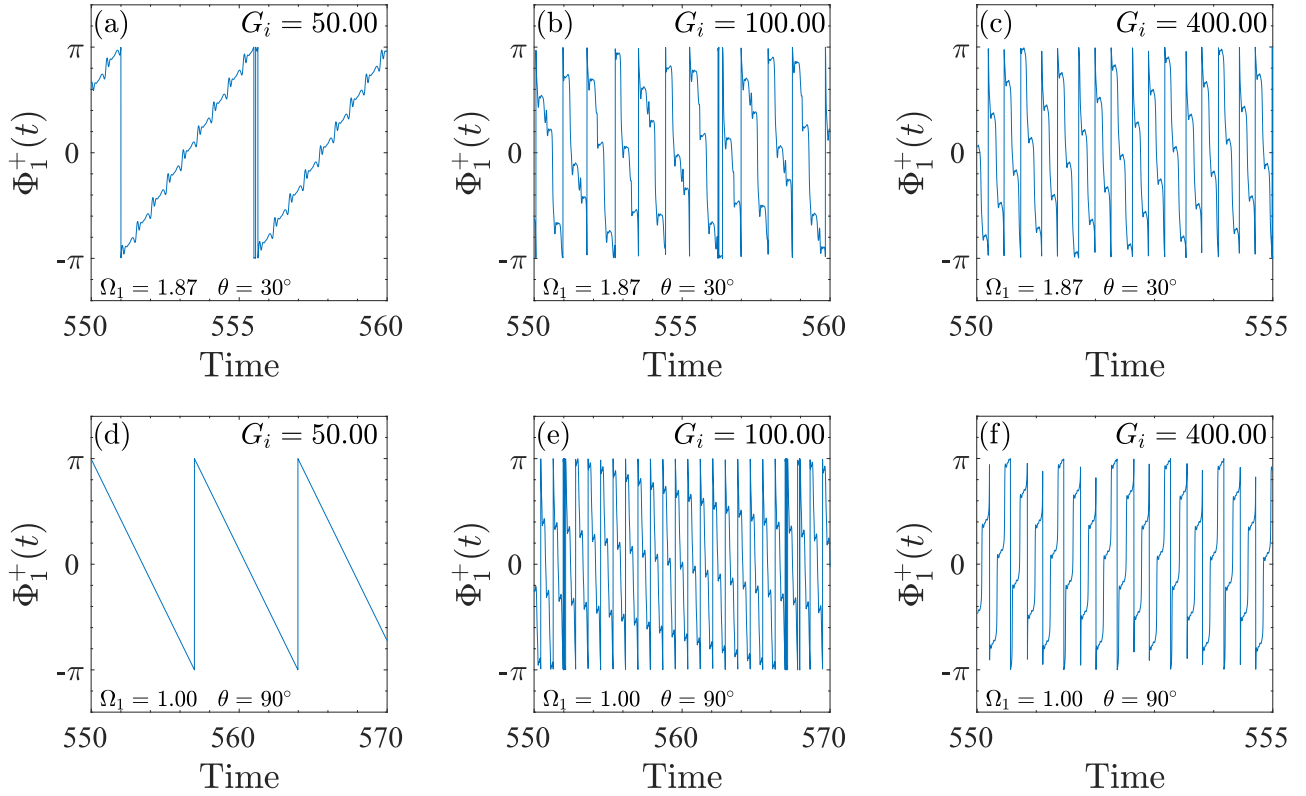


FIG. 10. Comparison of the temporal evolution of the phase  $\Phi_1(t)$  at  $\theta = 30^\circ$  (top row) and  $\theta = 90^\circ$  (bottom row), for three different magnetic forcing values:  $G_i = 50, 100, 400$ . The ambient field  $\mathbf{B}_0$  destroys the phase-locking period, and the phases becomes linearly dependent on time already at small  $G_i$ . For larger forcing, the precession accelerates, but the small perturbations act differently as  $\theta$  is varied.

the whole range of  $G_i$ , and the only structures emerging as the forcing increases are the secondary bifurcations, which survive up to  $G_i = 250$ .

Finally, since the presence of waves mainly affects the phases, it is interesting to investigate the temporal evolution of  $\Phi_n(t)^\pm$  for different  $\theta$ . The ambient field  $\mathbf{B}_0$  effectively destroys the phase-locking periods previously observed, because the phases now depend linearly on time already at small  $G_i$  (top-left panel of Fig. 10). Moreover, weak perturbations are superimposed on the phase structure, and disappear as  $\theta$  increases (bottom-left panel of Fig. 10). For larger forcing, the precession accelerates, but the small perturbations act differently as  $\theta$  is varied. An example for  $G_i = 100$  is visible in the two central panels of Fig. 10. For  $\theta = 30^\circ$  perturbations appear irregular, while for  $\theta = 90^\circ$  they form a regular temporal pattern. As  $G_i$  is increased further, for example at  $G_i = 400$  (corresponding to the quiescent zone in the case  $\Omega_n = 0$ , see Fig. 9), phase perturbations are always present, and for all angles they seem to follow a regular pattern (right panels of Fig. 10). In all cases, the phase-shift term of the PTC takes the functional form  $w_n(G, \theta) = S_n \hat{U}_n(0, \epsilon)$ .

## VI. CONCLUSIONS

The transition to chaos in a five-mode truncation of 2D MHD has been investigated, with and without background magnetic field, by means of complex variables. The dynamics of the system is of course strongly dependent on the external parameters. A complex fine structure of the various dynamical

regimes emerges as the parameters are changed. The simple model used here was able to capture various unexplored dynamical regimes that emerge for different parameters.

The main results described in this paper, potentially shared with a large class of nonlinear systems, may be summarized as follows.

(i) In the neutral flow case, the features of the system are similar to those observed using real variables [15,20]. The transition to a turbulent regime occurs via a Hopf bifurcation followed by a sequence of secondary period doubling bifurcations, compatible with the Feigenbaum prediction. For large external kinetic forcing, the system returns to a periodic structure.

(ii) The 2D MHD case corresponds to turbulence on the plane perpendicular to the background magnetic field. This is relevant to the nearly incompressible model of solar wind turbulence, where the superposition of 2D and slab fluctuations is assumed. In terms of Elsässer variables, the dynamics looks like hydrodynamics. However, in this case the transition to chaos, occurring through a Hopf bifurcation generating periodic orbits, is followed by the splitting in multiple subharmonic structures. These are incompatible with the Feigenbaum scenario, and disappear as the magnetic forcing increases. The process of splitting and merging of the orbits differs from the kinetic case. The process of subharmonics formation  $\rightarrow$  splittings  $\rightarrow$  shrinking is intermittently repeated up to a fully chaotic regime. Such behavior could be seen as an imitation of the frozen magnetic field lines, transported from large-scale fluid flow [38,60], which become

progressively more twisted as the magnetic Reynolds number increases [61].

(iii) In the fully chaotic regime, strange attractors appear. The phase-space dynamic is characterized by multiple subsystems with chaotic dynamics, or bundles of nonperiodic orbits. Moreover, despite the system entering into a fully chaotic zone, transition to a periodic orbit is intermittently observed, visible as periodicity windows in the bifurcation diagram. This dynamics may be seen as periods of self-organization of the flux tubes in MHD, e.g., the spaghetti-like random structures observed in space plasmas [37].

(iv) If the magnetic forcing is large enough, all subharmonic orbits start coalescing to a single stable periodic orbit, and the turbulence is finally suppressed. The coalescing structure observed in the bifurcation diagram shares similarities with the bubble structure discovered in double-diffusive convection and magnetoconvection [62,63]. The convective turbulence is gradually suppressed, and a quiescent state is reached via a Feigenbaum period halving, according to the process of period doubling  $\rightarrow$  turbulence  $\rightarrow$  period halving  $\rightarrow$  orbit coalescence. In our MHD case, neither the period halving nor the Feigenbaum conjecture are fulfilled. Instead, the coalescence occurs when two consecutive local maxima collapse to a single peak as the external forcing increases.

(v) By using the decomposition of the Elsässer variables in amplitudes and phases, the phase dynamics can be described by a simple PTC map. The phases of the fields are initially locked to piecewise constant periods, and a linear precession of phases is observed as the forcing increases. As the system enters the turbulent regime, a mixture of piecewise locked periods interrupted by intermittent periods of slight randomly modulated linear precession emerge. For larger forcing the phase locking is completely lost, and the phases dynamics is described by linear precession modulated by small random perturbations.

(vi) When a background external magnetic field has a component on the plane, the dynamics depends on the angle  $\theta$  between the selected wave vectors and the direction of the external field. When  $\theta$  is enclosed in the range  $0^\circ \leq \theta < \hat{\theta} \equiv 63.4^\circ$ , the dynamics is different from the previous MHD case: i.e., absence of an external field. In particular the turbulent region is stretched, in terms of the forcing range, showing its maximum extension for  $\theta \in [30^\circ, 60^\circ]$ , and the phase-locking periods do not appear because the phases are affected by the presence of linear waves that decorrelate the turbulent fluctuations. In those cases only a linear precession is present, whose speed increases with the forcing  $G_i$ . The main feature of this case is that for  $\theta \geq \hat{\theta}$  the transition to turbulence is gradually suppressed, and disappears for  $\theta = 90^\circ$  ( $\mathbf{B}_0 \parallel y$ ),

regardless of the value of  $G_i$ . The suppression of the turbulent regime at high  $\theta$  is likely related to the competition between decorrelation effects, induced by waves, and the nonlinear energy cascade.

It should be remarked that truncated models (fluid or MHD) do not contain, nor shall we be concerned with, the inertial or dissipative ranges of fully developed turbulence, whose description requires an infinite number of wave vectors. The emphasis on the chaotic dynamics of the MHD system presented here, should not be confused with fully developed turbulence, since the attractors of the truncated MHD system do not coincide with MHD turbulence as observed in space or laboratory plasmas. Similarly, the formation of the strange attractor should not be confused with the formation of a turbulent cascade, so that it is not immediately obvious one finds a counterpart of the chaotic dynamics in the observations of space plasmas turbulence, even if the stabilization of chaos, in the presence of an in-plane background magnetic field, is reminiscent of the fact that fully developed turbulent fluctuations lies in the plane perpendicular to the field.

A reader may reasonably ask what can be learned by approaching turbulence from a dynamical systems viewpoint [29,64]. The primary answer is that it demonstrates that there is no need to invoke singularities or noise to explain the complex dynamics observed in turbulence [64]. As a conclusion, the different route to chaos with respect to fluid turbulence, the coexistence of phase locking and free precession periods, and the suppression of turbulence due to decorrelation effects induced when a background magnetic is present, are interesting new features highlighted by the five-mode MHD model studied here. This could open new ways for investigating bifurcation to chaos in dynamical systems theory.

#### ACKNOWLEDGMENTS

F.C. acknowledges the contribution received from EU-H2020 program ERA-PLANET through the project “iGOSP” (Grant Agreement: 689443), funded under H2020-SC5-15-2015 “Strengthening the European Research Area in the domain of Earth Observation”, from FET Proactive project “I-Seed”, funded under Horizon 2020 research and innovation programme (Grant Agreement: 101017940), and from EU-H2020 project “EuroGEO Showcases: Applications Powered by Europe” (e-shape) (Grant Agreement: 820852), funded under H2020-SC5-2018-2 “Strengthening the benefits for Europe of the Global Earth Observation System of Systems (GEOSS) - establishing EuroGEO”. L.S.V. was funded by the Swedish Contingency Agency grant 2016-2102 and by SNSA grant 86/20.

- [1] E. N. Lorenz, Deterministic nonperiodic flow, *J. Atmos. Sci.* **20**, 130 (1963).  
 [2] D. Ruelle and F. Takens, On the nature of turbulence, *Commun. Math. Phys.* **20**, 167 (1971).  
 [3] E. Ott, *Chaos in Dynamical Systems*, 2nd ed. (Cambridge University Press, Cambridge, 2002).

- [4] V. Franceschini, C. Tebaldi, and F. Zironi, Fixed point limit behavior of n-mode truncated navier-stokes equations as n increases, *J. Stat. Phys.* **35**, 387 (1984).  
 [5] C. Foias, O. P. Manley, R. Temam, and Y. M. Treve, Asymptotic analysis of the navier-stokes equations, *Physica D* **9**, 157 (1983).

- [6] M. F. Doherty and J. M. Ottino, Chaos in deterministic systems: Strange attractors, turbulence, and applications in chemical engineering, *Chem. Eng. Sci.* **43**, 139 (1988).
- [7] P. Constantin, C. Foias, O. P. Manley, and R. Temam, Determining modes and fractal dimension of turbulent flows, *J. Fluid Mech.* **150**, 427 (1985).
- [8] J. P. Gollub and S. V. Benson, Many routes to turbulent convection, *J. Fluid Mech.* **100**, 449 (1980).
- [9] F. Carbone, H. Yoshida, S. Suzuki, A. Fujii, G. Strangi, C. Versace, and M. Ozaki, Clustering of elastic energy due to electrohydrodynamics instabilities in nematic liquid crystals, *Europhys. Lett.* **89**, 46004 (2010).
- [10] F. Carbone, L. Sorriso-Valvo, C. Versace, G. Strangi, and R. Bartolino, Anisotropy Of Spatiotemporal Decorrelation In Electrohydrodynamic Turbulence, *Phys. Rev. Lett.* **106**, 114502 (2011).
- [11] A. Liberzon, Y. Feldman, and A. Y. Gelfgat, Experimental observation of the steady-oscillatory transition in a cubic lid-driven cavity, *Phys. Fluids* **23**, 084106 (2011).
- [12] D. Faranda, Y. Sato, B. Saint-Michel, C. Wiertel, V. Padilla, B. Dubrulle, and F. Daviaud, Stochastic Chaos In A Turbulent Swirling Flow, *Phys. Rev. Lett.* **119**, 014502 (2017).
- [13] T. Cambonie, B. Moudjed, V. Botton, D. Henry, and H. Ben Hadid, From flying wheel to square flow: Dynamics of a flow driven by acoustic forcing, *Phys. Rev. Fluids* **2**, 123901 (2017).
- [14] F. Carbone, T. Alberti, L. Sorriso-Valvo, D. Telloni, F. Sprovieri, and N. Pirrone, Scale-dependent turbulent dynamics and phase-space behavior of the stable atmospheric boundary layer, *Atmosphere* **11**, 11040428 (2020).
- [15] C. Boldrighini and V. Franceschini, A five-dimensional truncation of the plane incompressible navier-stokes equations, *Commun. Math. Phys.* **64**, 159 (1979).
- [16] V. Franceschini and C. Tebaldi, A seven-mode truncation of the plane incompressible navier-stokes equations, *J. Stat. Phys.* **25**, 397 (1981).
- [17] V. Franceschini, Two models of truncated navier-stokes equations on a two-dimensional torus, *Phys. Fluids* **26**, 433 (1983).
- [18] N. Smaoui and M. Zribi, Dynamics and control of the seven-mode truncation system of the 2-d navier-stokes equations, *Commun. Nonlinear Sci. Numer. Simul.* **32**, 169 (2016).
- [19] H. Wang, Dynamical mechanism and energy conversion of the couette-taylor flow, *Int. J. Bifurcation Chaos* **29**, 1950100 (2019).
- [20] V. Franceschini and C. Tebaldi, Sequences of infinite bifurcations and turbulence in a five-mode truncation of the navier-stokes equations, *J. Stat. Phys.* **21**, 707 (1979).
- [21] Z.-M. Chen and W. Price, Transition to chaos in a fluid motion system, *Chaos, Solitons Fractals* **26**, 1195 (2005).
- [22] P. R. Fenstermacher, H. L. Swinney, and J. P. Gollub, Dynamical instabilities and the transition to chaotic taylor vortex flow, *J. Fluid Mech.* **94**, 103 (1979).
- [23] A. Brandstätter, J. Swift, H. L. Swinney, A. Wolf, J. D. Farmer, E. Jen, and J. P. Crutchfield, Low-Dimensional Chaos In A Hydrodynamic System, *Phys. Rev. Lett.* **51**, 1442 (1983).
- [24] A. Bishop, M. Forest, D. McLaughlin, and E. Overman, A quasi-periodic route to chaos in a near-integrable pde, *Physica D* **23**, 293 (1986).
- [25] R. Bruno and V. Carbone, *Turbulence in the Solar Wind*, 1st ed., Lecture Notes in Physics 928 (Springer International Publishing, Berlin, 2016).
- [26] G. P. Zank, L. Adhikari, P. Hunana, D. Shiota, R. Bruno, and D. Telloni, Theory and transport of nearly incompressible magnetohydrodynamic turbulence, *Astrophys. J.* **835**, 147 (2017).
- [27] G. P. Zank, M. Nakanotani, L.-L. Zhao, L. Adhikari, and D. Telloni, Spectral anisotropy in 2d plus slab magnetohydrodynamic turbulence in the solar wind and upper corona, *Astrophys. J.* **900**, 115 (2020).
- [28] J. W. Bieber, W. Wanner, and W. H. Matthaeus, Dominant two-dimensional solar wind turbulence with implications for cosmic ray transport, *J. Geophys. Res.: Space Phys.* **101**, 2511 (1996).
- [29] T. Bohr, M. H. Jensen, G. Paladin, and A. Vulpiani, *Dynamical Systems Approach to Turbulence*, Cambridge Nonlinear Science Series (Cambridge University Press, Cambridge, 1998).
- [30] V. Carbone and P. Veltri, Relaxation processes in magnetohydrodynamics - a triad-interaction model, *Astron. Astrophys.* **259**, 359 (1992).
- [31] R. D. Bartolo and V. Carbone, The role of the basic three-modes interaction during the free decay of magnetohydrodynamic turbulence, *Europhys. Lett.* **73**, 547 (2006).
- [32] M. Dobrowolny, A. Mangeney, and P. L. Veltri, Fully Developed Anisotropic Hydromagnetic Turbulence In Interplanetary Space, *Phys. Rev. Lett.* **45**, 144 (1980).
- [33] W. M. Elsässer, The hydromagnetic equations, *Phys. Rev.* **79**, 183 (1950).
- [34] C.-Y. Tu, E. Marsch, and K. M. Thieme, Basic properties of solar wind mhd turbulence near 0.3 au analyzed by means of elsässer variables, *J. Geophys. Res. Space Phys.* **94**, 11739 (1989).
- [35] Y. Zhou and W. H. Matthaeus, Non-wkb evolution of solar wind fluctuations: A turbulence modeling approach, *Geophys. Res. Lett.* **16**, 755 (1989).
- [36] R. Grappin, A. Mangeney, and E. Marsch, On the origin of solar wind mhd turbulence: Helios data revisited, *J. Geophys. Res. Space Phys.* **95**, 8197 (1990).
- [37] R. Bruno and V. Carbone, The solar wind as a turbulence laboratory, *Living Rev. Sol. Phys.* **10**, 2 (2013).
- [38] H. K. Moffatt, *Magnetic field generation in electrically conducting fluids*, Cambridge monographs on mechanics and applied mathematics (Cambridge University Press, Cambridge, 1983).
- [39] A. C. Ting, W. H. Matthaeus, and D. Montgomery, Turbulent relaxation processes in magnetohydrodynamics, *Phys. Fluids* **29**, 3261 (1986).
- [40] J. Lee, Triad-angle locking in low-order models of the 2d navier-stokes equations, *Physica D* **24**, 54 (1987).
- [41] T. G. Cowling, The magnetic field of sunspots, *Mon. Not. R. Astron. Soc.* **94**, 39 (1933).
- [42] J. Dormand and P. Prince, A family of embedded runge-kutta formulae, *J. Comput. Appl. Math.* **6**, 19 (1980).
- [43] H. Ernst, W. Gerhard, and P. N. Syvert, *Solving Ordinary Differential Equations I: Nonstiff Problems*, 2nd ed., Springer Series in Computational Mathematics 8 (Springer-Verlag, Berlin, 1993).
- [44] M. J. Feigenbaum, Quantitative universality for a class of nonlinear transformations, *J. Stat. Phys.* **19**, 25 (1978).
- [45] R. L. Devaney, M. W. Hirsch, and S. Smale, *Differential Equations, Dynamical Systems, and an Introduction to Chaos*, 3rd ed. (Elsevier Science, Amsterdam, 2013).
- [46] S. Haykin and Xiao Bo Li, Detection of signals in chaos, *Proc. IEEE* **83**, 95 (1995).

- [47] C. W. Wong, S.-W. Huang, and J. Wu, Ultrafast nonlinear dynamics in mesoscopic oscillators, in *Proceedings of the 4th International Conference on Applications in Nonlinear Dynamics (ICAND 2016)*, edited by V. In, P. Longhini, and A. Palacios (Springer International Publishing, Cham, 2017), pp. 93–100.
- [48] F. Peters, L. Lobry, and E. Lemaire, Experimental observation of Lorenz chaos in the Quincke rotor dynamics, *Chaos: An Interdisciplinary Journal of Nonlinear Science* **15**, 013102 (2005).
- [49] D. R. Moore, J. Toomre, E. Knobloch, and N. O. Weiss, Period doubling and chaos in partial differential equations for thermosolutal convection, *Nature (London)* **303**, 663 (1983).
- [50] H. E. Huppert and D. R. Moore, Nonlinear double-diffusive convection, *J. Fluid Mech.* **78**, 821 (1976).
- [51] L. N. D. Costa, E. Knobloch, and N. O. Weiss, Oscillations in double-diffusive convection, *J. Fluid Mech.* **109**, 25 (1981).
- [52] H. E. Huppert and J. S. Turner, Double-diffusive convection, *J. Fluid Mech.* **106**, 299 (1981).
- [53] B. Khesin, A. Givental, and V. I. Arnold, *Vladimir I. Arnold - Collected Works: Representations of Functions, Celestial Mechanics, and KAM Theory 1957–1965*, Vladimir I. Arnold - Collected Works (Springer, Berlin, 2010).
- [54] L. Glass and M. C. Mackey, A simple model for phase locking of biological oscillators, *J. Math. Biol.* **7**, 339 (1979).
- [55] H. Croisier, M. R. Guevara, and P. C. Dauby, Bifurcation analysis of a periodically forced relaxation oscillator: Differential model versus phase-resetting map, *Phys. Rev. E* **79**, 016209 (2009).
- [56] W. H. Matthaeus, S. Oughton, K. T. Osman, S. Servidio, M. Wan, S. P. Gary, M. A. Shay, F. Valentini, V. Roytershteyn, H. Karimabadi, and S. C. Chapman, Nonlinear and linear timescales near kinetic scales in solar wind turbulence, *Astrophys. J.* **790**, 155 (2014).
- [57] C. W. Smith, J. E. Stawarz, B. J. Vasquez, M. A. Forman, and B. T. MacBride, Turbulent Cascade At 1 au In High Cross-Helicity Flows, *Phys. Rev. Lett.* **103**, 201101 (2009).
- [58] L. Sorriso-Valvo, F. Catapano, A. Retinò, O. Le Contel, D. Perrone, O. W. Roberts, J. T. Coburn, V. Panebianco, F. Valentini, S. Perri, A. Greco, F. Malara, V. Carbone, P. Veltri, O. Pezzi, F. Fraternali, F. Di Mare, R. Marino, B. Giles, T. E. Moore, C. T. Russell, R. B. Torbert, J. L. Burch, and Y. V. Khotyaintsev, Turbulence-Driven Ion Beams In The Magnetospheric Kelvin-Helmholtz Instability, *Phys. Rev. Lett.* **122**, 035102 (2019).
- [59] P. Quijia, F. Fraternali, J. E. Stawarz, C. L. Vásconez, S. Perri, R. Marino, E. Yordanova, and L. Sorriso-Valvo, Comparing turbulence in a Kelvin-Helmholtz instability region across the terrestrial magnetopause, *Mon. Not. R. Astron. Soc.* **503**, 319 (2021).
- [60] H. K. Moffatt, Turbulence and stochastic processes: Kolmogorov's ideas 50 years on, *J. Fluid Mech.* **275**, 406 (1994).
- [61] L. Matilsky, S. Dyda, R. V. E. Lovelace, and P. S. Lii, Rossby vortices in thin magnetized accretion discs, *Mon. Not. R. Astron. Soc.* **480**, 3671 (2018).
- [62] E. Knobloch and N. O. Weiss, Bifurcations in a model of double-diffusive convection, *Phys. Lett. A* **85**, 127 (1981).
- [63] E. Knobloch and N. O. Weiss, Bifurcations in a model of magnetoconvection, *Physica D* **9**, 379 (1983).
- [64] U. Frisch, *Turbulence: the legacy of A. N. Kolmogorov* (Cambridge University Press, Cambridge, 1995).